NJC

Accepted Manuscript

This article can be cited before page numbers have been issued, to do this please use: J. Sun, P. wang and J. Chen, *New J. Chem.*, 2018, DOI: 10.1039/C8NJ04115F.

ROYAL SOCIETY OF CHEMISTRY

rsc.li/njc

DOI: 10.1039/C8NJ04115F

Journal Name

ARTICLE

Fe_2O_3 Hollow Microspheres as Highly Selective Catalysts to α-olefins

Received 00th January 20xx,
Accepted 00th January 20xx

DOI: 10.1039/x0xx00000x

www.rsc.org/

Jiaqiang Sun,* Pengfei Wang and Jiangang Chen*

We rationally designed and facile synthesized an excellent Fischer-Tropsch synthesis (FTS) catalyst based on mesoporous Fe_2O_3 microspheres derived from Fe–glycerate via an annealing treatment in air. The synthesis of Fe-containing precursor is the key step in the fabrication process of Fe_2O_3 microspheres with different interior structure (solid spheres, yolk-shell spheres and hollow spheres). The as-prepared catalysts have been characterized systematically to elucidate their structure-dependent catalytic property. The fine control of Fe_2O_3 with different interior structure and tunable pore size optimized distinctly the FTS activity and shifted the product distribution towards heavy hydrocarbons (especially, α-olefin) compared with the traditional iron catalysts. In light of the characterization results, the excellent FTS performance of Fe_2O_3 hollow spheres can be attributed to the hollow and mesoporous structures.

Introduction

Effectively controlling the architecture of the catalysts is important, because the activity and selectivity of catalysts depend greatly upon the surface/interface structure of the catalysts. [1] Particularly, hollow structures with a permeable outer shell bring many outstanding benefits to catalysis properties, in virtue of the large surface area, porosity, permeability [2] and internal void space. The high surface area and open porous channels of the hollow structures provide more accessible active sites for catalytic reaction. Hollow structures have recently emerged as ideal and powerful platforms for nanoreactors [3] and confined catalysis [4]. The design and preparation of heterogeneous catalysts with simultaneously enhanced activity and selectivity have attracted intense interest. [5] Low selectivity significantly limits the application of the Fischer-Tropsch process for synthesis of specific narrow hydrocarbon fractions. [6] The development of new strategies and novel catalysts that can tune the selectivity to desired products is an important goal for Fischer-Tropsch Synthesis (FTS). Considerable development has been achieved in recent years, but the effective control of product selectivity is still challenging. The previous studies have already demonstrated that the catalytic behaviors of catalysts are also strongly dependent on the diffusion of reactants and products in the pore of the catalyst support. [7] The diffusion limitation usually causes higher local H_2/CO ratios on the active metal surface because H_2 diffuses more quickly than CO, thus leading to a higher selectivity to CH_4. The small pore size usually shows lower heavy hydrocarbon selectivity. The large pore is able to diminish the diffusion resistance and lead to high heavy hydrocarbon content in the products, however, the large pore diameter mostly contains small surface area, resulting in low CO conversion levels. It suggests that the propagation of the carbon chain have close relationship with the pore size of the catalyst support. [8] However, these observations are generally the result of complex interplay among many factors induced by changing the pore size of the support. These factors include not only the confinement effect, which leads to changes in the re-adsorption probability of α-olefins in the confined spaces and the diffusion situation, but also the particle size effect, the reducibility and the dispersion of active species. These factors are all crucial in determining FT catalytic behavior. Bao and co-workers prepared Fe_2O_3 nanoclusters inside and outside carbon nanotubes (CNTs) with similar sizes and they found that the Fe_2O_3 nanoclusters confined inside CNTs were transformed into iron carbide species more efficiently. [9] But, the catalytic performance of catalysts is also dramatically affected by the metal–support interactions. [10] Thus, discussion on the sole effect of the pore size is quite difficult. The use of mesoporous materials with suitable pore size distributions directly as catalyst without support has provided some new insights into the pore size effect. The mesoporous catalysts with controllable pore diameters are suitable for the product of α-olefin, due to offering high specific surface area, short diffusion length of reaction gases, and efficient channels for mass transport. The mesopores may function as nanoreactor to control the chain length, either by shape selectivity or by enhancing the readsorption of intermediates. [11] In other words, the nanospaces of mesoporous materials can be expected to regulate the product selectivity. Therefore, the rational design

State Key Laboratory of Coal Conversion, Institute of Coal Chemistry, Chinese Academy of Sciences, Taiyuan, 030001, China
E-mail: sunjiaqiang@sxicc.ac.cn, chenjg@sxicc.ac.cn
Electronic Supplementary Information (ESI) available: See DOI: 10.1039/x0xx00000x

View Article Online
DOI: 10.1039/C8NJ04115F

and controllable synthesis of Fe_2O_3 hollow spheres with mesoporous structures are highly desirable for the enhancement of its catalytic performance but still remain as significant challenges. Recently, thermal decomposition of metal-containing precursor has been proved as a feasible route for preparing porous or hollow metal oxides micro/nanostructures owing to the facile modulation of the pore structure. [12] Therefore, the preparation of hollow structures using metal-containing precursor with large specific surface area, tunable framework and high porosity as precursors/templates may provide a unique opportunity to develop a new class of highly tailorable catalysts.

Herein, we report a simple, tunable and scalable Fe-containing precursor-mediated synthesis strategy for the preparation of highly uniform mesoporous Fe_2O_3 microspheres with different interior structure (solid spheres, yolk-shell spheres and hollow spheres). We then explore the interior structure and pore size effect of Fe_2O_3 for forming α-olefins in FTS. The feature of hollow and porous structures provides a larger surface area and more active sites to adsorb and activate reaction gases. As compared with conventional Fe_2O_3 nanoparticles, Fe_2O_3 hollow spheres with mesoporous structure exhibit excellent catalytic activity, higher α-olefin selectivity and higher stability. The excellent catalytic performance suggests that Fe_2O_3 hollow spheres are promising candidates for FTS catalysts. More importantly, the present study indicates that the hollow porous architectures can effectively enhance the performance of catalysts.

Results and discussion

Structural Characterization of metal-containing precursor and Fe_2O_3 microspheres

The fabrication process of Fe_2O_3 microspheres with different interior structure (solid spheres, yolk-shell spheres and hollow spheres) involves two steps. The one-pot self-templated formation of Fe–glycerate spheres is the key step to obtain high-quality Fe_2O_3 microspheres.

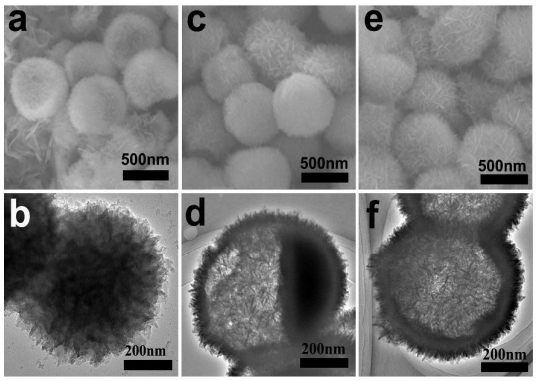

Figure 1. SEM and TEM images of the Fe–glycerate precursors after different reaction time: (a, b) 2 h; (c, d) 4 h; (e, f) 8 h.

The Fe–glycerate precursors with different interior structure (solid spheres, yolk-shell spheres and hollow spheres) were prepared by a one-pot solvothermal method. [13] To gain further insights into the fabrication process of the Fe-glycerate precursor spheres, a time-dependent morphology evolution study was conducted at 180 °C (Figure 1). The morphology of the Fe–glycerate precursor spheres obtained from different stages of solvothermal reaction has been investigated by SEM and TEM. At the early stage of the solvothermal reaction, solid spheres with thin nanoflakes (Figure 1a, b) are formed by the heterogeneous nucleation process. The as-prepared precursor spheres are highly uniform with a diameter of about 650 nm. Further extending the reaction time, it results in the partial hollowing of the pristine solid spheres (Figure 1c, d). Eventually after reaction for 8 h, the original solid spheres evolve into well-defined hollow spheres constructed by a large amount of radially standing nanosheets (Figure 1e, f). Representative TEM images (Figure 1f) further confirm the well-defined hollow structure with a shell thickness of around 150 nm. Along with morphology observations, the phase purity of the products was examined by XRD (Figure S1). All the peaks of the as-synthesized Fe–glycerate solid spheres, yolk-shell spheres and hollow spheres precursors can be well-indexed to the high crystal Fe–glycerate phase, which is a Fe-based alkoxide typically produced in glycerol. [13, 14]

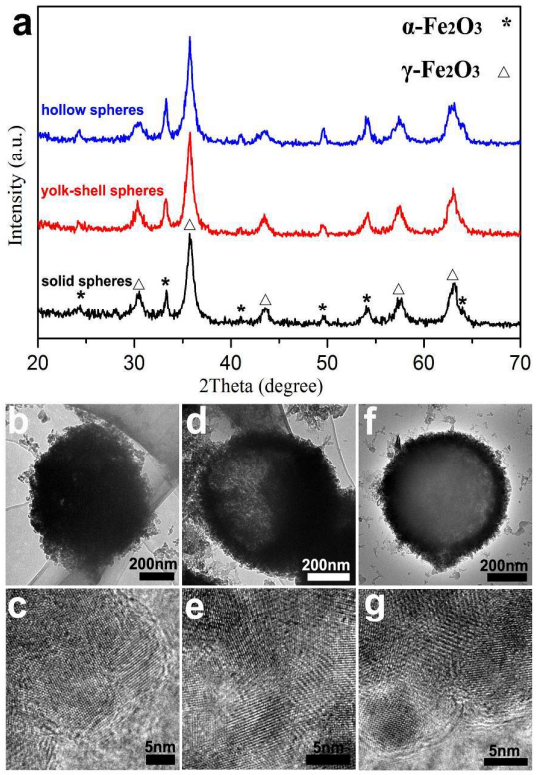

Figure 2. (a) XRD patterns of the Fe_2O_3 solid spheres, yolk-shell spheres and hollow spheres. TEM and HRTEM images of the Fe_2O_3 solid spheres (b, c), yolk-shell spheres (d, e) and hollow spheres (f, g)

View Article Online
DOI: 10.1039/C8NJ04115F

Figure 2a shows the XRD pattern of the as-prepared Fe_2O_3 sample after calcination at 350 °C for 3 h. All the peaks could be assigned to the α-Fe_2O_3 (JCPDS 33-0664) and γ-Fe_2O_3 (JCPDS 39-1346). For all catalysts, the crystallite size of α-Fe_2O_3 and γ-Fe_2O_3 was calculated from the reflection peak (104) at 2θ= 33.2 and the reflection peak (311) at 2θ= 35.6, respectively, according to the Scherrer equation. The particle sizes of α-Fe_2O_3 and γ-Fe_2O_3 are 19.5 nm and 10.9 nm for solid spheres, respectively. The particle sizes of α-Fe_2O_3 and γ-Fe_2O_3 are 21.0 nm and 11.1 nm for yolk-shell spheres, respectively. The particle sizes of α-Fe_2O_3 and γ-Fe_2O_3 are 20.5 nm and 10.9 nm for hollow spheres, respectively. As can be seen, the Fe_2O_3 crystalline size of the prepared catalysts is similar, indicating that the iron oxide particle size effect can be negligible. The Fe–glycerate precursors convert into Fe_2O_3 mesoporous spheres with well-retained structure after annealing in air (Figure 2b-g). As shown in Figure 2c, e, g, the Fe_2O_3 spheres are composed of interconnected nanoparticles. Highly crystalline Fe_2O_3 with different interior structure possess a highly porous texture, and their pores are clearly visible in the TEM images. HRTEM images further confirm the polycrystalline feature.

XPS was employed to identify the surface nature of the catalysts. The survey XPS spectra of the catalysts reveal that C, O, and Fe are the primary surface species (Figure 3a). Figure 3b shows the Fe 2p spectra of the catalysts. The peaks with BEs of 711.1 and 724.8 eV for the Fe $2p_{3/2}$ and $2p_{1/2}$ levels of Fe^{3+}, respectively, coupled with the satellite peak at ~719.0 eV, clearly verify the formation of α-Fe_2O_3. [15] While the Fe $2p_{3/2}$ peak at 710.4 eV and the Fe $2p_{1/2}$ peak at 724.0 eV are assigned to the γ-Fe_2O_3. [16] The signal of K could not be discerned in the spectrum of all the catalysts owing to the low K content. The amorphous C dominates the C 1s spectra of the catalysts (Figure S2), [17] which is beneficial to the homogeneous distribution of the iron oxide, and thus favoring the formation of the active surface iron carbide species upon exposure to syngas. [18] Because γ-Fe_2O_3 and Fe_3O_4 have very similar XRD patterns, we performed further characterization by the Mössbauer spectroscopy to distinguish the phases of iron oxide. Figure S3 show Mössbauer spectroscopy of mesoporous spheres after calcination. These original Mössbauer spectroscopy data of calcinated mesoporous spheres were fitted into a sextet and a doublet at 300 K. The analyzed results are summarized in Table S1. The phase of a sextet was considered as α-Fe_2O_3 from the isomer shift values relative to the α-Fe. The phase of a doublet was thought to be *γ*-Fe_2O_3 with superparamagnetic property at 300 K, which is a deficient inverse spinel. [19] Therefore, the mesoporous spheres were considered as a mixture of α-Fe_2O_3 and *γ*-Fe_2O_3 phase. Owing to the outstanding effect of potassium promotion on iron-based catalyst for FTS, namely improving activity and olefins to paraffins ratio, [20] all the catalysts contain a certain concentration of potassium. The K loading of Fe_2O_3 solid, yolk-shell and hollow spheres samples are 0.61, 0.63 and 0.67 wt%, respectively, according to the ICP-AES results.

The textural properties of the precursor and the catalysts were evaluated by N_2 adsorption-desorption isotherm measurement and were summarized in Table S2. The first pore was almost identical (about 3.5 nm) for the precursor, however, the second pore was different obviously (Figure S4). The bimodal precursor all displayed large specific surface area. All reported pores at 3.5 nm are the result of N_2 cavitation within the pores. BET surface area and total pore volume of the precursor with a distinct bimodal mesoporous structure increased from the solid spheres to hollow spheres, with the evolution of the microsphere interior structure. The pyrolysis of bimodal mesoporous Fe-glycerate precursor produces mesoporous Fe_2O_3 with a BET surface area of 78 for solid spheres, 87 for yolk-shell spheres, 92 m^2g^{-1} for hollow spheres, respectively. Compared with the precursor, the respective catalysts showed bigger average pore size and pore volume, which might be due to the gasification of organic ligands or collapse of the pore structure during thermal treatment in air. It could be also clearly observed the obviously different mesoporous distribution. It can be clearly seen that only one peak appears on the pore size distribution curves of the Fe_2O_3 spheres derived from the desorption branches using the Barett-Joyner-Halenda model (Figure S5). All the Fe_2O_3 catalysts clearly showed wider pore distribution and the average pore size of spheres increased with the increasing of hollow interiors.

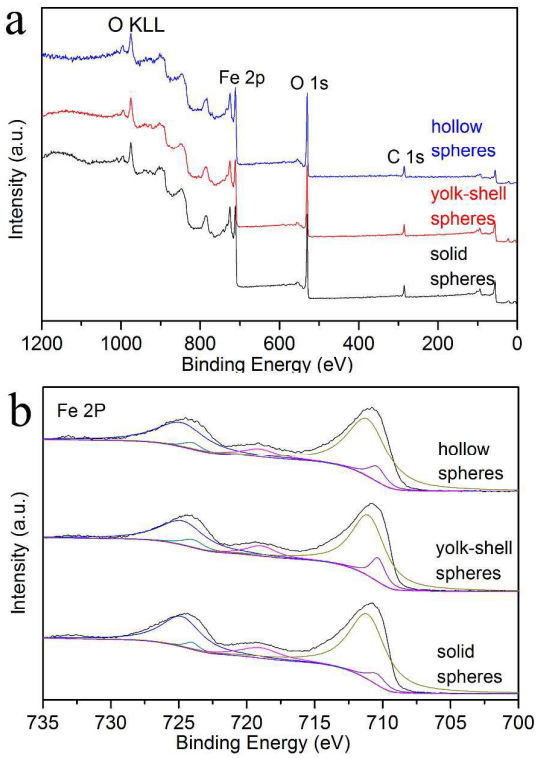

Figure 3. XPS survey spectra and Fe 2p XPS spectra of the Fe_2O_3 solid spheres, yolk-shell spheres and hollow spheres.

View Article Online
DOI: 10.1039/C8NJ04115F
ARTICLE Journal Name

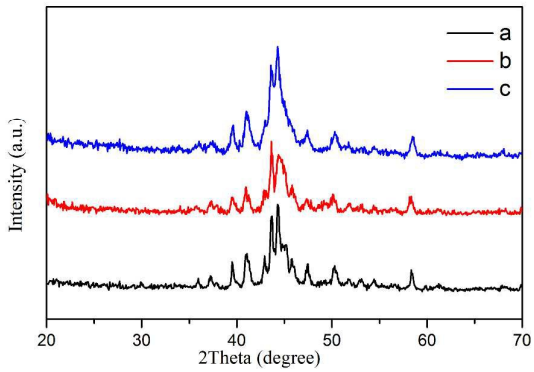

Figure 4. XRD patterns of the Fe_2O_3 solid spheres (a), yolk-shell spheres (b) and hollow spheres (c) catalysts after reduction.

The pores centered at around 15.0 nm were attributed to the mesoporous of the Fe_2O_3 solid spheres. While the average pore size of yolk-shell spheres and hollow spheres were 20.1 nm and 20.5 nm, respectively. The total pore volumes of the Fe2O3 solid spheres, yolk-shell spheres and hollow spheres were calculated to be 0.33 cm^3 g^{-1}, 0.39 cm^3 $g^{-1}$and 0.44 cm^3 g^{-1}, respectively. The Fe_2O_3 hollow spheres with the largest pore size showed the highest BET surface area and the largest pore volumes than that of others. The data suggested that the pore structure of catalyst was not completely destroyed and still present mesoporous structure. Therefore, Fe-glycerate with large specific surface area, tunable framework and high porosity have been considered as more promising templates or precursors to fabricate mesoporous iron oxides catalysts, primarily via thermolysis.

The reduction behavior of the Fe_2O_3 mesoporous microspheres was investigated by H_2-TPR and the profiles are shown in Figure S6. All catalysts showed similar reduction behavior that consisted of two distinctive steps. The low-temperature peak was due to the reduction of γ-Fe_2O_3 and α-Fe_2O_3 to Fe_3O_4; the reduction at above 400 °C consisted of heavily overlapped peaks corresponding to the consequential reduction of Fe_3O_4 (Fe_3O_4 to FeO and FeO to metallic Fe). [21] This facile reduction of γ- Fe_2O_3 is of utmost importance in chemical reactions. [21]The reduction temperature of γ-Fe_2O_3 shifted from 323 °C for the solid spheres to 315 °C for the hollow spheres in the low-temperature region.

Catalytic Properties

Prior to the FTS reaction, the Fe_2O_3 spheres were activated in CO at 300 °C for 16 h. After reduction, all the peaks in the XRD pattern shown in Figure 4 can be indexed as the monoclinic phase Hägg carbide (Fe_5C_2, JCPDS 20-0508), with no other phase being detected, indicating the Fe_2O_3 catalyst was fully carburized. The Fe_2O_3 mesoporous microspheres catalysts were tested under the industrially relevant conditions of 280 °C, 2.0 MPa, H_2/CO ratio of 2 and GHSV of 10 $Lg^{-1}h^{-1}$. The catalytic activities and hydrocarbon products distribution (expressed as C-mol% on a carbon basis) for the Fe_2O_3

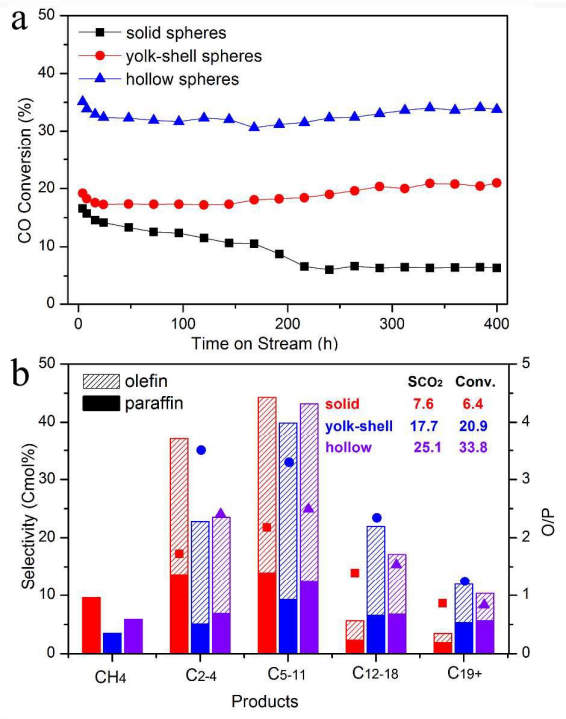

Figure 5. (a) Plots of CO conversion of the Fe_2O_3 solid spheres, yolk-shell spheres and hollow spheres against time on stream. (b) Hydrocarbon product selectivity of the catalysts after 400 h on stream at 2.0 MPa, 280°C, H_2/CO = 2 and GHSV = 10 $Lg^{-1}h^{-1}$.

mesoporous microspheres after 24 h of reactions are summarized in Table S3. Furthermore, relevant data from literature for other iron catalysts are also listed in the Table 2. [22] The catalysts prepared by the Fe-containing precursor-mediated synthesis route display much higher FTY and excellent C_{5+} selectivity in comparison with others catalysts. FTY of the yolk-shell and hollow spheres after 24 h of reactions is about 8.7 and 14.0 μmol $CO g_{Fe}^{-1}s^{-1}$, respectively, which indicates that the full hollow structure of spheres is more favorable to the catalytic activity than the partial hollow structure of spheres. This remarkable difference is related to the different internal structure that affects the carbidization degree upon exposure to syngas. The time on stream evolution of CO conversion for the catalysts is presented in Figure 5a, thereby providing insights in the stability of these catalysts. The initial CO conversion with the solid spheres catalysts was 16.6% and decreased to 6.6% after FTS for 216 h, then remaining stable. The CO conversion of the yolk-shell and hollow spheres catalysts after activation exhibited an initial decrease slightly in the induction period and they displayed steady-state operation after 24 h on stream. The CO conversion of the yolk-shell spheres catalysts was 17.3% in the steady state. The hollow spheres catalysts realized the CO conversion of 33.8% during the 400 hours of reaction. We attribute these results to their different internal space that can act as nanoreactor. The difference found as a consequence of different structure is the activity and stability of the catalyst.

View Article Online
DOI: 10.1039/C8NJ04115F

One of the most important requirements for an FTS catalyst is to obtain the maximum production of the heavy hydrocarbon fraction (especially, α-olefins) while suppressing methane selectivity to the lowest level possible. The hydrocarbon selectivity of the Fe_2O_3 spheres after 400 h on stream is shown in Figure 5b. The hollow spheres catalysts showed high selectivity toward heavy hydrocarbon products (C_{5+}, 70.6%) while yielding a methane product fraction lower than 6%. The selectivity of C_{5-11} (gasoline fraction) and C_{12-18} hydrocarbons (diesel fraction) for the hollow spheres catalysts are 43.2 % and 17.1 %, respectively, which is desirable for their application in the FTS process.

The yolk-shell spheres catalysts also exhibited high selectivity to C_{5+} (~73.7%) while comparatively little methane (3.5%). The selectivity of C_{5-11} (gasoline fraction) for the yolk-shell spheres is 39.9%, while the selectivity of C_{12-18} is 21.9 %. In particular, the α-olefin (in the C_{5+} hydrocarbons) fraction amounted to 51.6% and 45.9% for the yolk-shell and hollow spheres in all the hydrocarbon products, respectively. This is higher than the values reported to date for iron catalysts, including the Fe_xO_y@C spheres [22d], Fe-rGO, [22e], Fe_5C_2 nanoparticles, [23a] and other catalysts derived from the pyrolysis of metal–organic frameworks (Fe_3O_4@Fe_5C_2 core-shell nanoparticles and Fe@C). [24] The C_{2-4} and C_{5-11} (gasoline fraction) hydrocarbons become dominant for the solid spheres catalysts. The solid spheres catalysts with a small amount of the diesel fraction displayed a high selectivity to methane (~9.6%). The CO_2 selectivity evolves in a trend from 7.6% for the solid spheres catalyst to 25.1% for the hollow spheres catalyst. Moreover, the selectivity did not undergo significant changes during the whole reaction period for the Fe_2O_3 mesoporous microspheres. As the BET results (Table S2, Figure S7) shown, the average pore size of the spheres used was increased after FTS reaction, ensuring better accessibility of the embedded iron species to the reactants. But the solid spheres may caused more blocking pore, which hindered reactants to approach the active sites, leading to lower CO conversion rates and higher methane. The catalyst with appropriate larger pore size showed higher middle distillate selectivity, especially the yolk-shell spheres catalyst showed higher C_{5-18} selectivity. Furthermore, the formation of CH_4 was remarkably suppressed with increasing pore size. It could also be seen that the yolk-shell sphere and hollow sphere catalyst with larger mesoporous size showed higher olefin selectivity, which was better than that of the solid sphere. The high α-olefin selectivity of the yolk-shell and hollow spheres catalyst was likely due to its larger mesoporous size, which could favors the desorption of olefin and diffusion of reactants and production. [25] The mesoporous catalysts typically possess high surface areas and controllable pore diameters, which are suitable for the preparation of heavy hydrocarbons. The ratio of olefin to paraffin (denoted as O/P) for the solid spheres, the yolk-shell spheres and the hollow spheres in the C_5-C_{11} range hydrocarbons is 2.2, 3.3 and 2.5, respectively. As illustrated by Figure 5b, the O/P ratio in hydrocarbon decreases with increasing chain length (n>5) for all the catalysts.

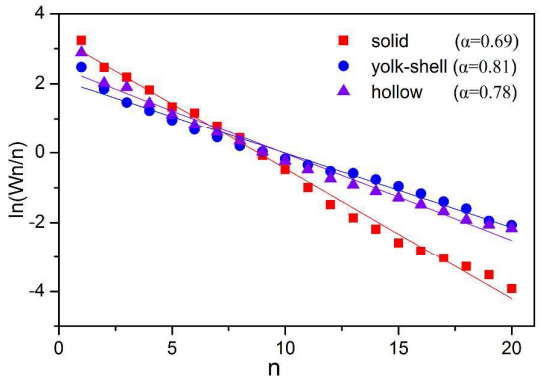

Figure 6. ASF distribution plots for the catalysts after 400 h on stream at 2.0 MPa, 280°C, H_2/CO = 2 and GHSV = 10 $Lg^{-1}h^{-1}$. n is the number of carbon atoms in a product, and Wn is the weight fraction of the product with carbon number equal to n.

It is clear from Figure 6 that the hydrocarbons selectivity for all the catalysts follow the Anderson–Schulz–Flory (ASF) distribution, with the α value of 0.78 for the hollow spheres catalysts, similar to that obtained with the yolk-shell sphere catalysts, while the solid sphere catalyst presents the lower α value of 0.69. This can be rationalized from the simplified "surface carbide" or "carbene insertion-paraffin-metal ring coordination intermediates" mechanism, which is widely accepted for FTS. [26] In this model, methylene generated by CO dissociation hydrogenation and metal form the first paraffin-metal ring coordination. The carbon chain grows by the insertion of methylene monomer units (CH_2) to the adsorbed paraffin-metal ring coordination. The methylene insertion process will be affected by the space steric hindrance of cyclic coordination, making methylene easier to attack α site. The chain growth is terminated by forming α-olefins or by hydrogenation to produce paraffins. The hollow spheres catalysts provides probably more CO chemisorptions and larger space, which promoting markedly the product shifting towards heavy hydrocarbons (especially, α-olefin) by improving the carbon-chain growth. The lower methane selectivity can be expected when using the K modified yolk-shell and hollow sphere catalysts with larger pore diameter that favour the chain growth and the termination step. [27] The hollow spheres catalysts showed high catalytic activities combined with high selectivities to the desired products. It should be point out that the reaction performance of this catalyst should be the synergetic effects of pore size and structure.

Active Phase in FTS

The structural and chemical phase characterization of the catalysts was carried out after 400 h on stream in FTS. The cubic phase Fe_3O_4 (JCPDS 65-3107) and the monoclinic phase Hägg carbide (Fe_5C_2, JCPDS 20-0508) appear in the XRD patterns for the catalysts used (Figure S8). While the diffraction peak at 24.3° marked with triangle is readily assignable to C, which was mainly caused by the carbon

View Article Online
DOI: 10.1039/C8NJ04115F
ARTICLE Journal Name

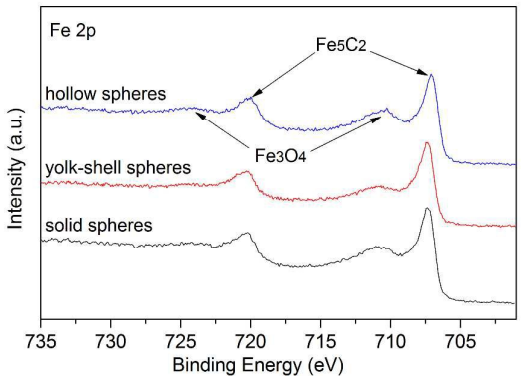

Figure 7. Fe 2p XPS spectra of the Fe_2O_3 solid spheres, yolk-shell spheres and hollow spheres after 400 h on stream.

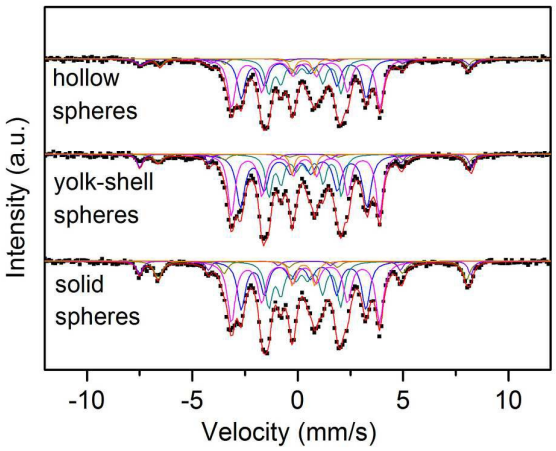

Figure 8. Mössbauer spectra of the Fe_2O_3 solid spheres, yolk-shell spheres and hollow spheres after 400 h on stream.

deposition. The peaks at 707.4 and 720.2 eV in the Fe 2p XPS spectrum (Figure 7) also demonstrate the existence of Fe_5C_2. [23] The presence of two weak peaks at 710.8 and 724.3 eV in all samples indicated the existence Fe_3O_4, suggesting that the surface of the iron carbide was slightly oxidized. [23a] Mössbauer spectroscopy is powerful to identify and quantify the iron phases formed in FTS. Hence, to further identify the active phases of the FTS catalysts, the phases of iron specie were also then determined by Mössbauer spectroscopy. Figure 8 presents the ^{57}Fe Mössbauer spectrum of all the catalysts after 400h of FTS and the deconvoluted subspectra; the corresponding fitting parameters are listed in Table S4.

The asymmetric line shapes of the Mössbauer spectroscopy of mesoporous spheres after FTS is mainly due to defective crystal structure. Mössbauer spectrum results revealed that all the catalysts used attained similar iron carbide species. Iron carbides are generally acknowledged as the main active phase in FTS, among which, Hägg carbide (χ-Fe_5C_2) and cementite (θ-Fe_3C) are mostly reported as heterogeneous catalysts for FTS. Iron carbides (ε'-$Fe_{2.2}C$, ε-Fe_2C) are identified active at low temperature. [28] In the present work, the catalysts were mainly converted to χ-Fe_5C2 and ε'-$Fe_{2.2}C$. Fe_3O_4 was also found after 400 h of FTS, which was mainly caused by the gradual oxidation of the iron carbide phase with the water produced upon exposure to syngas. [29] However, after 400 h of synthesis gas treatment, the solid spheres exhibit lower ε'-$Fe_{2.2}C$ contents (25%) compared to the hollow spheres (29%). The lower degree of total carbides and the higher content of Fe_3O_4 for the solid spheres could directly result in relatively lower catalytic activities and worse stability. [30] The hollow spheres are more favorable to the exposure of iron species on the catalyst compared with the solid spheres. In addition, the hollow spheres facilitates the reduction and carburization of Fe_2O_3 compared to the solid spheres, promoting the formation of carbonaceous species in surface layers.

Conclusions

In summary, we develop a facile solvothermal approach combined with subsequent calcination to synthesize highly uniform Fe_2O_3 mesoporous microspheres. Dedicate control over the synthesis of Fe–glycerate precursors will result in Fe_2O_3 spheres with many structure-induced merits. Compared to other iron catalysts, the mesoporous materials typically possess high surface areas and controllable pore diameters, which are suitable for the preparation of heavy hydrocarbons (especially, α-olefin). With the high structural integrity, complex interior architectures, and enlarged surface area, the hollow Fe_2O_3 microspheres exhibit superior catalytic performances for FTS. It is implied that exploiting the unique structural transformation of Fe–glycerate precursors, thus controlling pore size and structure of Fe_2O_3, is an efficient method to prepare highly active, selective and stable FTS catalysts.

Experimental

Catalyst Preparation.

0.404 g of $Fe(NO_3)_3{\cdot}6H_2O$, 0.025 g of $K(NO_3)_3$ and 15 mL of glycerol were dissolved in 105 mL of isopropanol under magnetic stirring. After stirring for 10 min, 1 mL of deionized water was added into the above solution. The homogeneous solution prepared above was transferred directly into a 200 mL Teflon-lined stainless steel autoclave and maintained at 190 °C for 2h, 4h or 8 h. After cooling to room temperature naturally, the precipitate was separated by centrifugation, washed with several times with ethanol and dried at 80 °C for 4 h. The as-obtained Fe-glycerate precursor was then calcinated at 350°C for 4h in air with a heating rate of 1.0 °Cmin^{-1}.

Characterization

Powder X-ray diffraction (XRD) was performed on a Shimadzu XRD-6000 diffractometer with Cu Kα radiation (λ= 1.5418 Å) in the 2θ range from 10° to 70°. The morphology of as-synthesized samples were monitored by using a scanning electron microscope (SEM, Zeiss Supra 55). The structure and

DOI: 10.1039/C8NJ04115F

composition of the products were characterized by means of a high-resolution transmission electron microscope (HRTEM, JEM 2100F) and X-ray photoelectron spectroscopy (XPS, ESCALAB 250). The content of K was also analyzed by inductively coupled plasma atomic emission spectroscopy (ICP-AES, Thermo iCAP6300). The surface area was determined by a Tristar Ⅱ3020 N_2 adsorption analyser. The precursor (50 mg) was placed in a quartz reactor and was reduced by a 5% H_2/N_2 gas mixture at a flow rate of 50 mL/min, as the TPR experiments were performed. MES experiments were carried out in an MR-351 constant acceleration Mössbauer spectrometer (FAST, Germany) drive with a triangular reference signal at room temperature. Data analysis was performed using a non-linear least-squares fitting routine that modeled the spectra as a combination of quadruple doublets, and magnetic sextets based on a Lorentzian line shape profile. The components were identified based on their isomer shift (IS), quadruple splitting (QS), and magnetic hyperfine fields (Hhf). The magnetic hyperfine fields were calibrated with the 330 kOe field of α-Fe at ambient temperature.

Catalytic Reaction

The catalytic behaviour was investigated in a fixed bed reactor. 1.0 g of catalyst was diluted with 1 mL of quartz powder (60–80 mesh). The produced catalysts were reduced at 300 °C and 0.2 MPa for 16 h by CO with a gas hourly space velocity (GHSV) of 5 $Lg^{-1}h^{-1}$. After in-situ reduction, the reactor was cooled to 50 °C, the synthesis gas (n_{H2}/n_{CO}=2, GHSV = 10 $Lg^{-1}h^{-1}$) was fed into the catalysts bed and the temperature was increased at 1.0 °$Cmin^{-1}$ heating rate to 280 °C. During testing, the pressure of synthesis gas was maintained at 2.0 MPa, and the reaction products passed a 130 °C hot trap and a 5 °C cooling trap at working pressure. The composition of the reactants and tail gas were analyzed online by gas chromatography (GC). The CO, CO_2, CH_4 and N_2 were analyzed by using a carbon molecular sieve column and thermal conductivity detector (TCD). The light hydrocarbons were analyzed using a capillary porapak-Q column with a flame ionization detector (FID). The oil and wax were analyzed offline using GC with an OV-101 capillary column and an FID. The catalytic activity, expressed as iron time yield (FTY), was expressed as moles of CO converted to hydrocarbons per gram of Fe per second. The hydrocarbon selectivities were calculated on a carbon basis with the exception of CO_2. An average of 3% and a maximum of 5% mass and carbon balance errors were calculated for the run.

Conflicts of interest

There are no conflicts to declare.

Acknowledgements

This work was financially supported by the National Natural Science Foundation of China (No.21503256 and 21373254) and the autonomous research project of SKLCC (No. 2013BWZ004).

Notes and references

1 a) B. Xiao, Z. Niu, Y.-G. Wang, W. Jia, J. Shang, L. Zhang, D. Wang, Y. Fu, J. Zeng, W. He, K. Wu, J. Li, J. Yang, L. Liu and Y. Li, *J. Am. Chem. Soc.*, 2015, **137**, 3791-3794; b) K. Zhou, Y. Li, *Angew. Chem. Int. Ed.* **2012**, *51*, 602-613; c) X. Mou, B. Zhang, Y. Li, L. Yao, X. Wei, D. S. Su and W. Shen, *Angew. Chem. Int. Ed.* **2012**, *51*, 2989 –2993.

2 R. Ameloot, F. Vermoortele, W. Vanhove, M. B. Roeffaers, B. F. Sels and D. V. De Vos, *Nat. Chem.* **2011**, *3*, 382-387.

3 J. Liu, H. Q. Yang, F. Kleitz, Z. G. Chen, T. Yang, E. Strounina, G. Q. Lu and S. Z. Qiao, *Adv. Funct. Mater.* **2012**, *22*, 591-599.

4 J. B. Joo, M. Dahl, N. Li, F. Zaera and Y. Yin, *Energy Environ. Sci.* **2013**, *6*, 2082-2092.

5 G. A. Somorjai, J. Y. Park, *Angew. Chem., Int. Ed.* **2008**, *47*, 9212–9228.

6 J. Wang, H. Li, D. Li, J. P. D. Breejen and B. Hou, *RSC Adv.* 2015, **5**, 65358-65364.

7 H. Becker, R. Guttel, T. Turek, *Catal. Sci. Technol.* **2016**, *6*, 275-287.

8 Y. Liu, J. F. Chen, Y. Zhang, *RSC Adv.* **2015**, *5*, 29002-29007.

9 W. Chen, Z. Fan, X. Pan, X. Bao, *J. Am. Chem. Soc.* **2008**, *130*, 9414-9419.

10 a) S. O. Moussa, L. S. Panchakarla, M. Q. Ho, M. S. El-Shall, *ACS Catal.* **2014**, *3*, 535-545; b) R. P. Mogorosi, N. Fischer, M. Claeys, E. van Steen, *J. Catal.* **2012**, *289*, 140-150; c) B. Sun, K. Xu, L. Nguyen, M. Qiao, F. Tao, *ChemCatChem* **2012**, *4*, 1498-1511.

11 C. M. Parlett, K. Wilson, A. F. Lee, *Chem. Soc. Rev.* **2013**, *42*, 3876-3893.

12 a) L. Hu, Q. Chen, *Nanoscale* **2014**, *6*, 1236-1257; b) W. Xia, A. Mahmood, R. Zou, Q. Xu, *Energy Environ. Sci.* **2015**, *8*, 1837-1866; c) L. Zhang, H. B. Wu, X. W. Lou, *J. Am. Chem. Soc.* **2013**, *135*, 10664–10672.

13 F. X. Ma, H. Hu, H. B. Wu, C. Y. Xu, Z. Xu, L. Zhen and X. W. Lou, *Adv. Mater.* **2015**, *27*, 4097-4101.

14 L. Shen, L. Yu, X. Y. Yu, X. Zhang and X. W. Lou, *Angew. Chem. Int. Ed.* **2015**, *54*, 1868-1872.

15 a) J. Sun, Y. Chen, J. Chen, *Catal. Commun.* **2017**, *91*, 34-37; b) T. Yamashita, P. Hayes, *Appl. Sur. Sci.* **2008**, *254*, 2441-2449; c) S. Bharathi, D. Nataraj, M. Seetha, D. Mangalaraj, N. Ponpandian, Y. Masuda, K. Senthil, K. Yong, *Crystengcomm* **2010**, *12*, 373-382.

16 X. Zhang, Y. Niu, X. Meng, Y. Li, J. Zhao, *CrystEngComm* **2013**, *15*, 8166-8172.

17 Y. Cheng, J. Lin, K. Xu, H. Wang, X. Yao, Y. Pei, S. Yan, M. Qiao, B. Zong, *ACS Catal.* **2016**, *6*,389−399.

18 V. P. Santos, T. A. Wezendonk, A. I. Dugulan, M. A. Nasalevich, H. U. Islam, A. Chojecki, S. Sartipi, X. Sun, A. A. Hakeem, A. C. Koeken, M. Ruitenbeek, T. Davidian, G. R. Meima, G. Sankar, F. Kapteijn, M. Makkee and J. Gascon, *Nat. Commun.* **2015**, *6*, 6451-6458.

19 a) K. Woo, J. Hong, S. Choi, H. W. Lee, J. P. Ahn, C. S. Kim, W. L. Sang, *Chem. Mater.* **2004**, *16*, 2814-2818; b) E. Tronc, A. Ezzir, R. Cherkaoui, C. Chanéac, M. Noguès, H. Kachkachi, D. Fiorani, A. M. Testa, J. M. Grenèche and J. P. Jolivet, *J. Magn. & Magn. Mater.* **2000**, *221*, 63-79.

20 H. M. Torres Galvis, K. P. de Jong, *ACS Catal.* **2013**, *3*, 2130–2149.

21 a) J. Zielin´ski, I. Zglinicka, L. Znak, Z. Kaszkur, *Appl. Catal., A* **2010**, *381*, 191–196; b) X. Mou, X. Wei, Y. Li, W. Shen, *Crystengcomm* **2012**, *14*, 5107-5120.

22 a) J. Sun, Y. Chen, J. Chen, *Catal. Sci. Technol.* **2016**, *6*, 7505–7511; b) J. Tu, M. Ding, Y. Zhang, Y. Li, T. Wang, L. Ma, C. Wang, X. Li, *Catal. Commun.* **2015**, *59*, 211–215; c) Y. Liu, J. Chen, J. Bao, Y. Zhang, *ACS Catal.*, **2015**, *5*, 3905–3909; d) G. Yu, B. Sun, Y. Pei, S. Xie, S. Yan, M. Qiao, K. Fan, X. Zhang and B. Zong, *J. Am. Chem. Soc.* **2010**, *132*, 935-937; e) B. Sun, Z.

View Article Online
DOI: 10.1039/C8NJ04115F

Jiang, D. Fang, K. Xu, Y. Pei, S. Yan, M. Qiao, K. Fan and B. Zong, *Chemcatchem* **2013**, *5*, 714-719.
23 C. Yang, H. Zhao, Y. Hou, D. Ma, *J. Am. Chem. Soc.* **2012**, *134*, 15814–15821; b) S. Y. Hong, D. H. Chun, J. I. Yang, H. Jung, H. T. Lee, S. Hong, S. Jang, J. T. Lim, C. S. Kim, J. C. Park, *Nanoscale* **2015**, *7*, 16616-16620.
24 a) B. An, K. Cheng, C. Wang, Y. Wang, W. Lin, *ACS Catal.* **2016**, *6*, 3610-3618; b) T. A. Wezendonk, V. P. Santos, M. A. Nasalevich, Q. S. E. Warringa, A. I. Dugulan, A. Chojecki, A. C. J. Koeken, M. Ruitenbeek, G. R. Meima, H. U. Islam, G. Sankar, M. Makkee, F. Kapteijn, J. Gascon, *ACS Catal.* **2016**, *6*, 3236-3247.
25 H. Xiong, Y. Zhang, S. Wang, J. Li, *Catal. Commun.* **2005**, *6*, 512-516.
26 M.E. Dry, *Appl. Catal.* **1996**, *138*, 319-344.
27 C. Wang, L. Xu, Q. Wang, *J. Nat. Gas Chem.* **2003**, *12*, 10-16
28 a) E. de Smit, B.M. Weckhuysen, *Chem. Soc. Rev.* **2008**, *37*, 2758-2781; b) B. Sun, J. Lin, K. Xu, Y. Pei, S. R. Yan, M. H. Qiao, X. X. Zhang, B. N. Zong, *ChemCatChem* **2013**, *5*, 3857−3865.
29 M.K. Gnanamani, G. Jacobs, H.H. Hamdeh, W.D. Shafer, B.H. Davis, *Catal. Today* **2013**, *207*, 50-56.
30 S. Z. Li, R. J. O'Brien, G. D. Meitzner, H. Hamdeh, B. H. Davis, E. Iglesia, *Appl. Catal., A* **2001**, *219*, 215–222.

View Article Online
DOI: 10.1039/C8NJ04115F

Fe_2O_3 Hollow Microspheres as Highly Selective Catalysts to α-olefins

Jiaqiang Sun,* Pengfei Wang and Jiangang Chen*

State Key Laboratory of Coal Conversion, Institute of Coal Chemistry, Chinese Academy of Sciences, Taiyuan, 030001, China

TOC

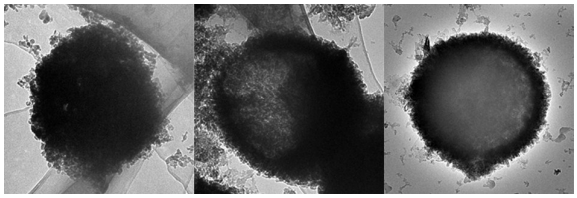

Fe_2O_3 derived from Fe–glycerate with different interior structure and tunable pore size optimized distinctly the product selectivity.